



Simple synthesis of anatase/rutile/brookite TiO₂ nanocomposite with superior mineralization potential for photocatalytic degradation of water pollutants



Renata Kaplan^a, Boštjan Erjavec^a, Goran Dražić^b, Jože Grdadolnik^c, Albin Pintar^{a,*}

^a Laboratory for Environmental Sciences and Engineering, National Institute of Chemistry, Hajdrihova 19, SI-1001 Ljubljana, Slovenia

^b Laboratory for Materials Chemistry, National Institute of Chemistry, Hajdrihova 19, SI-1001 Ljubljana, Slovenia

^c Laboratory for Biomolecular Structure, National Institute of Chemistry, Hajdrihova 19, SI-1001 Ljubljana, Slovenia

ARTICLE INFO

Article history:

Received 4 June 2015

Received in revised form 3 August 2015

Accepted 12 August 2015

Available online 14 August 2015

Keywords:

Titanium dioxide

Highly ordered anatase/rutile/brookite

nanocomposite

Photocatalysis

Water treatment

ABSTRACT

In this study, we report a simple synthesis procedure of anatase/rutile/brookite TiO₂ nanocomposite material, designed for efficient transformation of emerging water pollutants (e.g., bisphenol (A)) to CO₂ and H₂O as final products of complete photo-oxidation. Sol–gel procedure with a subsequent hydrothermal treatment carried out at mild temperature and in the presence of 3 M HCl led to the formation of TiO₂ nanomaterial, which consists of anatase (43%), rutile (24%) and brookite (33%) polymorph phases within the same material. For the purpose of efficient evaluation of nanocomposite activity, individual polymorphs of anatase, rutile and brookite were also prepared using the same precursor material. Individual polymorph phases within the nanocomposite material crystallized separately and formed mixed agglomerates; the polymorphs were regularly shaped and randomly distributed in agglomerates, where some of the anatase particles exhibited truncated octahedron morphology, rutile was in the form of tetragonal prisms with pyramidal termination and brookite was shaped as blocky particles, which were found to be the smallest within the nanocomposite material (~20 nm). Newly synthesized TiO₂ nanocomposite was highly active in terms of mineralization, since after 60 min of irradiation under UV light almost 60% of water dissolved pollutant bisphenol A was successfully transformed into CO₂ in H₂O. On the other hand, the benchmark TiO₂ P25 Degussa catalyst reached a lower extent of mineralization, which is due to significantly less expressed resistance to accumulation of carbonaceous deposits on the catalyst surface.

© 2015 Elsevier B.V. All rights reserved.

1. Introduction

Titanium dioxide (TiO₂) is the most widely used semiconductor material, which is due to the wide variety of its applications in the field of optics, cosmetics and solar cells [1–5]. It is an abundant, cheap and non-toxic material, with a high prospective for addressing environmental concerns. It can mainly be found in three different crystalline forms: anatase, rutile and brookite. Anatase adopts a tetragonal structure in which four edges are shared per octahedron, but there is no corner sharing. Similarly, rutile also has a tetragonal structure in which two opposite edges of octahedron are shared in order to form a linear chain along [001] direction. Further, chains are joined through corner connections. Brookite has an orthorhombic structure where octahedrons share

three edges as well as corners [6]. Rutile is known to be the stable form, while anatase and brookite are metastable and can be transformed to rutile when heated [7,8]. Anatase is commonly known as the most active phase and is therefore extensively used in the variety of photocatalytic applications [9–15]. Its high activity is directly connected to prolonged lifetime of charge carriers (conduction band electrons and valence band electron vacancies) and spatial charge separation [16]. The excited electrons are reducing agents, responsible for formation of superoxide radical ions (•O₂[−]) with dissolved O₂, and the holes left in the valence band can react with adsorbed water (or surface hydroxyls) to form very reactive hydroxyl radicals (•OH). The latter have been considered to be the major active species participating in photocatalytic oxidation (PCO) reactions. Owing to their short lifetimes (usually 10^{−9} s), several indirect detection methods have been developed, which rely on the measurement of probe molecules introduced in the medium. The products of reaction between the probe molecules and •OH radicals give measurable and lasting signals, which can be detected

* Corresponding author. Fax: +386 1 47 60 460.
E-mail address: albin.pintar@ki.si (A. Pintar).

with diverse analytical techniques (e.g., electron paramagnetic resonance (EPR), UV–vis absorption spectroscopy, luminescence and fluorescence) [17,18].

Since efficiency of the photocatalytic process is largely limited by unfavorable electron-hole recombination, coupling two different types of photoactive semiconductor materials can have a beneficial effect on enhancing electron-hole charge separation, thus inhibiting rapid recombination of excited electrons with valence band electron vacancies [19]. Anatase/rutile nanocomposites are most widely investigated [20–22], while fewer reports have been made on anatase/brookite [23] and brookite/rutile [24] solids. Most widely studied anatase/rutile nanocomposite is TiO₂ P25 Degussa (Evonik) (phase composition in ratio of 80/20 for anatase/rutile), as a result of its superior activity in the wide variety of applications [25–27]. On the other hand, reports in the open literature dealing with the preparation of TiO₂ nanocomposites which consist of all three polymorphs, are extremely rare. Liao et al. [19] reported that the anatase/rutile/brookite nanocomposite can be prepared under solvothermal conditions, where brookite and anatase phases crystallize into irregular nanoparticles and rutile phase into single-crystalline particles. The material prepared by these authors exhibited high activity for the photocatalytic degradation of aqueous methyl orange dye solution. However, there are no reports existing on the photocatalytic behavior of regularly shaped three-phase mixed oxides with approximately equal shares of respective phases (i.e., anatase, rutile, brookite).

Photocatalytic activity of the prepared anatase/rutile/brookite TiO₂ nanocomposite was evaluated using a priority pollutant bisphenol A (BPA), which is a representative of endocrine disrupting compounds (EDCs). BPA is a toxic aromatic compound known to interfere with normal hormone functions and therefore poses a threat to aquatic life as well as humans [28]. Its widespread (detected in seven out of ten investigated landfill leachates in concentrations ranging from non-detectable to 17.2 mg/l [29]) and harmful nature makes it an appropriate candidate for a test compound in advanced oxidation processes (AOPs) like heterogeneous photocatalytic oxidation. In the present study, the preparation and thorough characterization of anatase/rutile/brookite nanocomposite is highlighted. The coexisting mixture of anatase/rutile/brookite phases was prepared using a simple ultrasound assisted sol–gel procedure with a subsequent hydrothermal treatment. The obtained material with regularly shaped and crystalline particles exhibited high potential toward BPA mineralization which is, in the process of heterogeneous photocatalytic oxidation, superior even to that of TiO₂ P25 Degussa.

2. Experimental

2.1. Synthesis of catalysts

The precursor material was synthesized using ultrasound assisted sol–gel technique. First, a certain amount of titanium (IV) isopropoxide (Sigma–Aldrich, ≥97.0%) (TTIP) was added dropwise to 50 ml of 2-propanol (Sigma–Aldrich, p.a., ≥99.8%) under vigorous stirring. The formed mixture was sonicated using an ultrasonic bath in order to ensure optimal distribution of TTIP in 2-propanol. Subsequently, urea (Kemika, ≥99.5%) was added in molar ratio of TiO₂:urea = 1.1:1 in order to induce the formation of crystal lattice defects [30]. To achieve optimal mixing of all the present compounds, the mixture was again subjected to sonication. The obtained sol was converted into gel by dropwise addition of distilled water under vigorous mixing. After the hydrolysis, stepwise preparation procedure was continued with sonication in order to achieve formation of localized hot spots by collapse of bubbles due

to cavitation [31]. The as-prepared precursor material was dried at 60 °C in an oven for 18 h.

Anatase/rutile/brookite TiO₂ nanocomposite material (ARB) as well as the pure polymorphs of TiO₂ (anatase (A), rutile (R) and brookite (B)) were synthesized using hydrothermal synthesis route under different pH values of solutions. For ARB, the precursor material was added to 3 M HCl (Merck, 37.0%), sonicated and thoroughly mixed. The as-obtained suspension was hydrothermally treated in Teflon-lined autoclave for 24 h at 175 °C. The resulting white material was filtered and thoroughly washed with distilled water. In order to preserve the structure, the material was dried in vacuum under cryogenic conditions for 24 h. Pure phases of anatase (A), rutile (R) and brookite (B) were prepared using the same precursor material that was used for the preparation of ARB. For the preparation of anatase, precursor was added to 0.001 M H₃PO₄ (Merck, 85.0%) and hydrothermally treated in Teflon-lined autoclave for 24 h at 180 °C. Rutile was prepared hydrothermally with 4 M HCl (Merck, 37.0%) at 200 °C for 2 h. Brookite was the only material which was prepared under basic conditions. The synthesis was carried out at 200 °C for 72 h in a Teflon-lined autoclave in the presence of 0.1 M NaOH (Merck, ≥99.0%). The synthesized polymorphs were further filtered, thoroughly washed with distilled water and dried in vacuum under cryogenic conditions for 24 h.

2.2. Characterization of the prepared materials

The as-prepared materials were characterized by means of scanning electron microscopy (SEM) (Carl Zeiss, model FE-SEM SUPRA 35VP) and transmission electron microscopy (TEM) (JEOL, model ARM 200CF). X-ray powder diffraction patterns were acquired using PANalytical X'pert PRO MPD diffractometer with Cu Kα1 radiation (1.54056 Å) in reflection geometry. Data collection was conducted in the range between 15 and 85° (steps of 0.034°). Specific surface area, total pore volume and average pore size were determined by measuring nitrogen adsorption and desorption isotherms at –196 °C (Micromeritics, model TriStar II 3020). BET (Brunauer, Emmett, Teller) theory was applied in order to calculate the specific surface area, while pore size distribution was calculated from the desorption branch of the corresponding nitrogen isotherms, employing the BJH method. Diffuse reflectance UV–vis spectra of the prepared materials were recorded using a UV–vis spectrophotometer (PerkinElmer, model Lambda 650). Samples were scanned with the speed of 120 nm/min and slit set to 4 nm. Background correction was performed using a white reflectance standard (Spectralon®). Acidic properties of synthesized materials were determined by means of temperature programmed desorption (TPD) analysis using Pyris 1 TGA instrument (PerkinElmer). Samples were heated at 180 °C for 120 min under N₂ flow to eliminate surface impurities and then cooled down to room temperature, followed by the surface saturation with *n*-propylamine. The excess of probe molecule was then removed in N₂ flow. TPD of *n*-propylamine was carried out by heating samples to 750 °C at 10 °C/min. Raman spectra were recorded on a Bruker Ram II FT Raman spectrometer by applying laser excitation at 785 nm. Typically, laser power during the sample examination was set to 200 mW. Raman scattered light was detected with a TE Si-avalanche pin diode detector. 1024 interferograms were averaged and apodized with Happ–Genzel function. Spectra were recorded in the spectral range between 3000 and 75 cm^{–1} with the nominal resolution of 4 cm^{–1}. The amount of carbon accumulated on the surface of examined solids during photocatalytic experiments was determined by means of CHNS elemental analysis (PerkinElmer, model 2400 Series II).

2.3. Photolytic and photocatalytic oxidation experiments

Photolytic and photocatalytic degradation of BPA ($c_0 = 10$ mg/l in ultrapure water with $18.2\text{ M}\Omega\text{ cm}$ resistance) was studied in a 250 ml batch slurry reactor at atmospheric pressure. The reactor unit was thermostated at $T = 20^\circ\text{C}$ (Julabo, model F25/ME), magnetically stirred (600 rpm) and continuously sparged with purified air (45 l/h). The catalyst concentration was in the range of 0–125 mg/l (photolytic and photocatalytic experiments, respectively). Before adding the catalyst into the model aqueous solution, the powders were suspended by means of ultrasonification. Prior to the illumination period, the suspension was kept in dark (30 min) to allow establishing of sorption equilibrium. The reactor content was illuminated by high pressure UVA mercury lamp (150 W, maximum at $\lambda = 365$ nm). The lamp was positioned in a water cooling jacket placed vertically in the center of the slurry reactor unit. Representative 2-ml aqueous-phase samples for subsequent HPLC (to follow temporal BPA concentration) and total organic carbon (TOC) analyses were periodically collected from the reaction suspension in predetermined time intervals and filtered through a membrane filter (Sartorius, $0.45\text{ }\mu\text{m}$) in order to remove catalyst particles.

3. Results and discussion

3.1. Catalyst characterization

SEM images (Fig. 1a and b) of ARB nanocomposite sample indicate that the ultrasound assisted sol–gel synthesis followed by the hydrothermal treatment led to the formation of well-developed and randomly distributed nanoparticles with average size of 50 nm. Pure anatase (sample A) was found in the form of nanofibers (Fig. 1c), while rutile (sample R) possessed the shape of humming-tops in micron size, which were composed of smaller nanocrystals (Fig. 1d). Finally, brookite (sample B) was formed in the shape of curved nanocrystals, approximately 200 nm in length and about 100 nm in diameter (Fig. 1e).

TEM micrographs are presented in Fig. 2. SAED (selected area electron diffraction) pattern is displayed in Fig. 2a, showing the presence of all three variants of crystalline TiO_2 : anatase (A), rutile (R) and brookite (B). The strongest line at 0.32–0.35 nm (first circle from the central spot) consisted of overlapping spots of anatase (101), brookite (210) and rutile (110) planes. Each of these surfaces is also the most stable of the other facets in a particular polymorph, following the sequence for the surface energies: rutile (110) \approx anatase (101) < brookite (210) [32]. The second circle is characteristic for brookite (211) plane. Remaining lines (circles) could be assigned to other planes of anatase, rutile and brookite. From the intensity of non-overlapping lines like rutile (101), anatase (200) and brookite (210), we can conclude that the volume ratio of three phases is approximately the same. Based on the intensity of individual spots and the broadening of the circles we can say that the size of prepared particles is in the 50 nm range. Most of the particles were slightly rounded and elongated with an approximate aspect ratio of 1.5. The size of these particles (measured at longer axis) was from 30–70 nm. TEM micrograph of all three phases present in the ARB sample is displayed in Fig. 2b. Using SAED it was revealed that the rounded particles were anatase and the blocky particles were brookite. During the study it was found that brookite particles were the most beam-sensitive of all particles. Beside rounded and blocky particles also elongated larger particles with aspect ratio around 10 were detected, which are, according to SAED analysis, rutile. Some of the anatase particles (presented in Fig. 2c, including 3D shape reconstruction) exhibit truncated octahedron morphology, which is the most stable shape of this polymorph. Terminal planes in the octahedron are of (101)

Table 1

Specific surface area (S_{BET}), total pore volume (V_{pore}), average pore width (d_{pore}) and average crystallite size of the prepared materials and commercial TiO_2 P25 Degussa sample.

Material	S_{BET} (m^2/g)	V_{pore} (cm^3/g)	d_{pore} (nm)	Crystallite size (nm)		
				Anatase	Rutile	Brookite
Anatase	137	0.42	10.6	11.4		
Rutile	8	0.03	11.5		35.0	
Brookite	25	0.08	12.5			57.7
ARB	32	0.14	13.9	a	69.0	35.6
TiO_2 P25 Degussa	52	0.15	10.2	23.0	35.0	

^aCrystallite size of anatase in ARB sample could not be determined due to the overlapping of anatase (101), brookite (120) and brookite (111) diffraction peaks.

type and truncation is on basal (001) planes. Rutile particles were in the form of tetragonal prisms with pyramidal termination. Prismatic terminal planes are of (110) type and the pyramidal planes of (111) type. They are presented in Fig. 2d, together with 3D reconstruction of shape. HAADF (high angle annular dark field) image of brookite particle with indicated terminal planes and reconstructed 3D shape is presented in Fig. 2e. From the obtained data we can conclude that individual polymorph phases crystallized separately and formed mixed agglomerates.

BET specific surface area (S_{BET}), together with total pore volume (V_{pore}) and average pore diameter (d_{pore}) of ARB nanocomposite, along with the pure TiO_2 polymorphs (samples A, R and B), are presented in Table 1. It can be noted that the synthesis of materials at extremely low pH values (4 M HCl, pH -0.63 ; 3 M HCl, pH -0.45) led to the formation of materials exhibiting low BET specific surface area (R and ARB samples, respectively), while 0.001 M H_3PO_4 with pH value equal to 2.94 had a positive effect on the development of specific surface area (sample A). Namely, the nanofibrous morphology of anatase exhibited BET specific surface area of $137\text{ m}^2/\text{g}$. On the contrary, brookite particles synthesized in alkali solution exhibited BET specific surface of $25\text{ m}^2/\text{g}$, which was closer to BET surface area of ARB and R samples.

Fig. 3a represents XRD diffraction patterns of pure polymorphs (anatase, rutile and brookite). Crystallite size of the individual TiO_2 phase was determined by means of Scherrer equation from characteristic XRD diffraction peaks: (101) for anatase ($2\theta = 25.3^\circ$), (110) for rutile ($2\theta = 27.4^\circ$) and (121) for brookite ($2\theta = 30.8^\circ$). XRD examination of ARB sample (Fig. 3b) shows a diffraction pattern, which can clearly be ascribed to a three-phase mixed TiO_2 nanocomposite that consists of anatase, rutile and brookite nanocrystals. The obtained XRD diffractogram of ARB sample adequately covers all relevant reflections of the individual phases present. The phase content of each polymorph can be determined from integrated intensities of anatase (101), rutile (110) and brookite (121) peaks, using the below presented equations [33]:

$$W_a = \frac{K_a A_a}{K_a A_a + A_r + K_b A_b} \quad (1)$$

$$W_r = \frac{A_r}{K_a A_a + A_r + K_b A_b} \quad (2)$$

$$W_b = \frac{K_b A_b}{K_a A_a + A_r + K_b A_b} \quad (3)$$

where W_a , W_r and W_b represent mass fractions of anatase, rutile and brookite, respectively. A_a , A_r and A_b correspondingly represent the integrated intensities for each polymorph. K_a and K_b stand for correction coefficients, which have values of 0.886 and 2.721 [33], respectively. Due to the overlap of anatase (101) peak with brookite (120) and (111) peaks, a numerical deconvolution technique was used to separate these peaks. Calculations performed show that the prepared ARB nanocomposite material consists mostly of anatase (43%), while the portions of rutile and

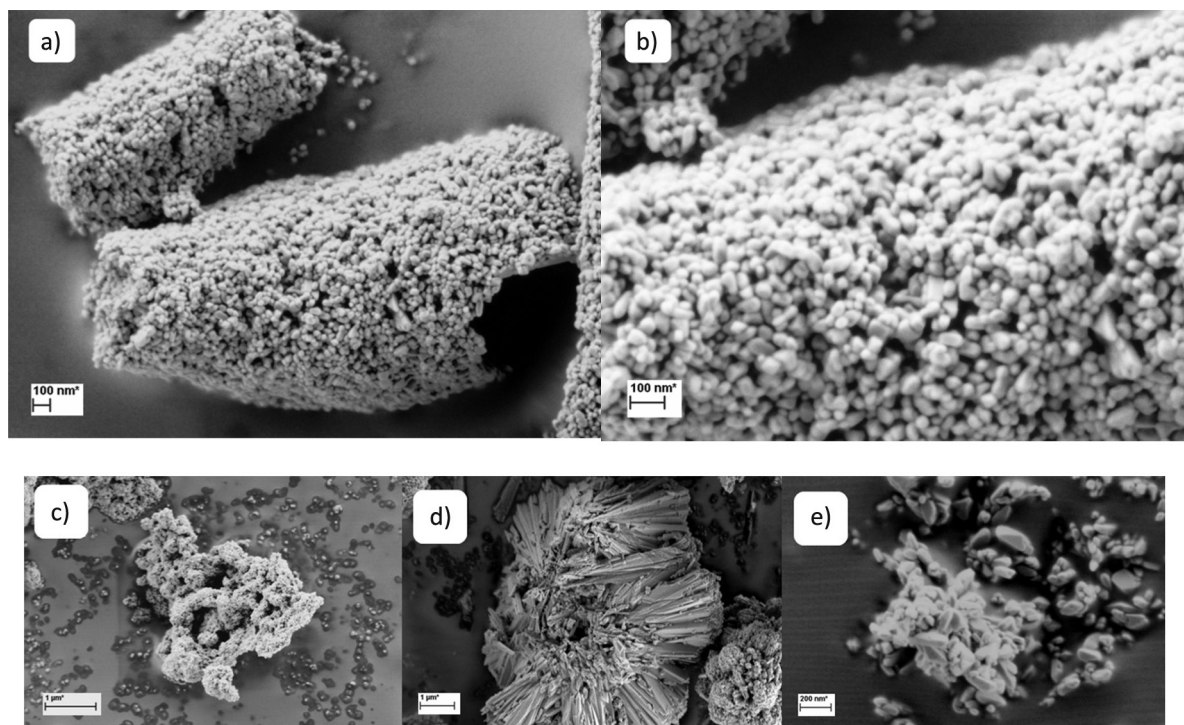


Fig. 1. SEM micrographs of (a) and (b) anatase/rutile/brookite TiO_2 nanocomposite (ARB); (c) anatase (A); (d) rutile (R) and (e) brookite (B).

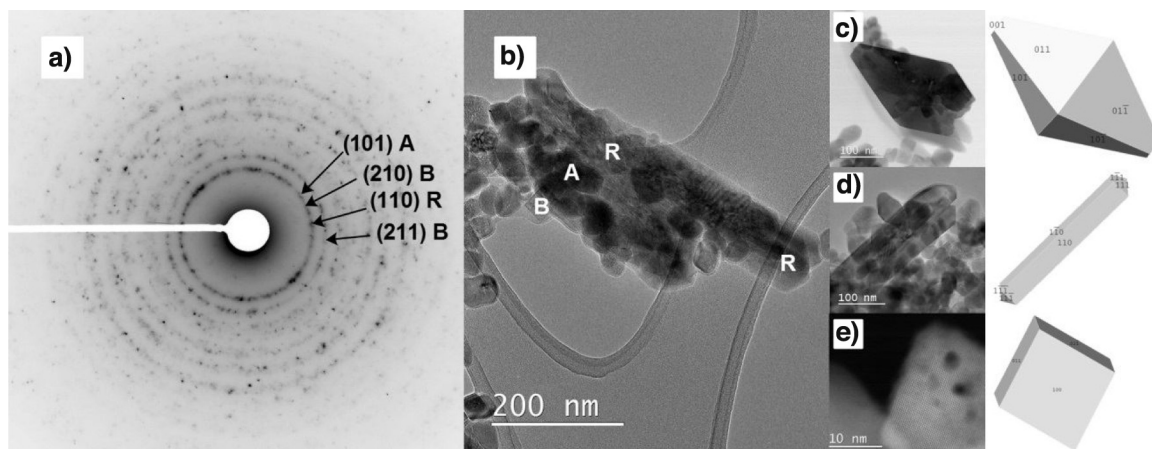


Fig. 2. (a) SAED pattern of anatase/rutile/brookite TiO_2 (ARB) nanocomposite; (b) TEM micrograph of all three phases present in ARB; (c) HR-TEM micrograph of anatase with truncated octahedron morphology and its 3D shape reconstruction; (d) HR-TEM micrograph of prismatic rutile particle with reconstructed 3D shape and (e) HAADF image of brookite particle with indicated terminal planes and reconstructed 3D shape.

brookite equal to 24 and 33%, respectively. Theoretical BET value of the prepared ARB nanocomposite material, which can be calculated using data presented in Table 1 (BET specific surface areas of anatase, rutile and brookite) and mass fractions of the respective singular phases within ARB, amounts to $69 \text{ m}^2/\text{g}$. It is obvious that BET specific surface area of ARB ($32 \text{ m}^2/\text{g}$) is not simply a linear combination of contributions of singular polymorphs.

The phase composition of ARB sample was further explored by Raman spectroscopy. The results are illustrated in Fig. 4, which shows the spectra of pure anatase, rutile, brookite and the investigated ARB nanocomposite. The Raman lines for pure anatase at 148 , 409 , 515 and 635 cm^{-1} are assigned to the E_g , B_{1g} , A_{1g} (or B_{1g}) and E_g modes of the anatase phase, respectively [34]. The strongest E_g mode at 148 cm^{-1} is attributed to the external vibration of the anatase structure. The most distinctive peaks for pure rutile appear at 448 and 610 cm^{-1} and are ascribed to E_g and A_{1g} modes of the

rutile phase [34]. Brookite is known to exhibit a relatively complex vibrational spectrum (Fig. 4) when compared to other TiO_2 polymorphs, but is identified with a very strong band at around 150 cm^{-1} [35]. The Raman spectrum of ARB sample clearly confirmed the coexistence of all three singular polymorphs, since all vibrations could be identified with intensities of particular TiO_2 polymorph.

Optical properties of the prepared materials were characterized using UV–vis diffuse reflectance spectroscopy. Kubelka–Munk analysis of the corresponding diffuse reflection spectra is presented in Fig. 5. Band gap energies for pure anatase, rutile and brookite samples were found to be equal to 3.50 , 3.00 and 3.30 eV , respectively. In the case of ARB sample, which is composed of all three polymorphic phases of TiO_2 , it was measured to be 3.28 eV . We also demonstrated that theoretical band gap of nanocomposite materials could be accurately determined using the XRD data (i.e., mass

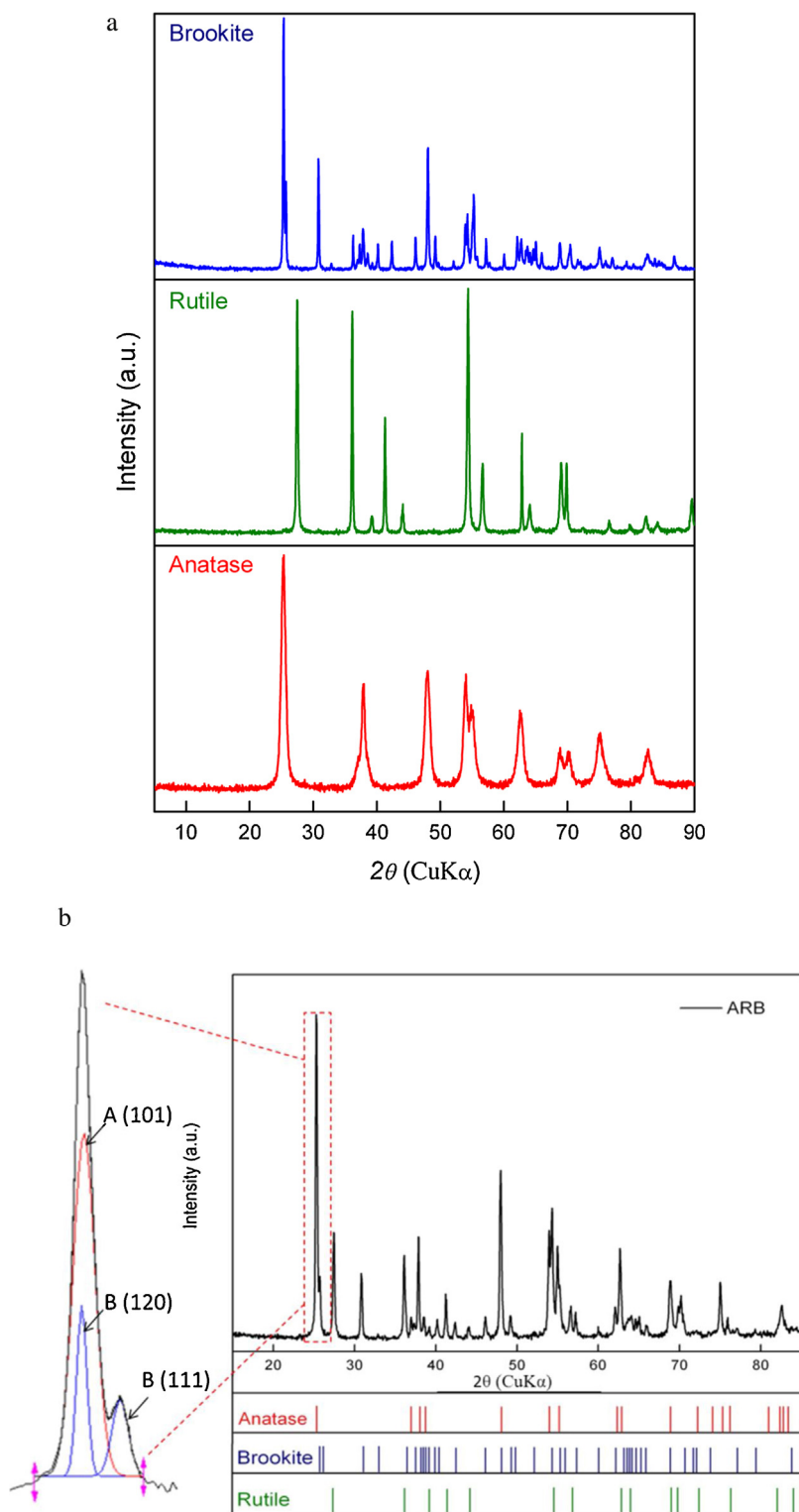


Fig. 3. XRD diffractograms of (a) anatase, rutile, brookite and (b) anatase/rutile/brookite (ARB) nanocomposite.

fraction of each polymorph) and band gap energies of individual polymorphs (anatase, rutile, brookite), and applying Eq. (4). In the latter, E_g represents band gap energy for each material (A = anatase, R = rutile, B = brookite, ARB = anatase/rutile/brookite nanocomposite), while W_A , W_B and W_R represent mass fractions of anatase, rutile and brookite within the prepared ARB material.

$$E_g(\text{ARB}) = E_g(\text{A})W_A + E_g(\text{R})W_R + E_g(\text{B})W_B \quad (4)$$

Theoretically determined band gap energy was equal to 3.32 eV, which is in good agreement with the above-mentioned experimental value. This alludes that certain autonomy of polymorph phases within the ARB sample takes place, but this can only be taken as a rough estimation, since electronic properties of pure polymorphs can, due to the preparation procedures applied, be much different to those of ARB. To conclude, the obtained data is of great

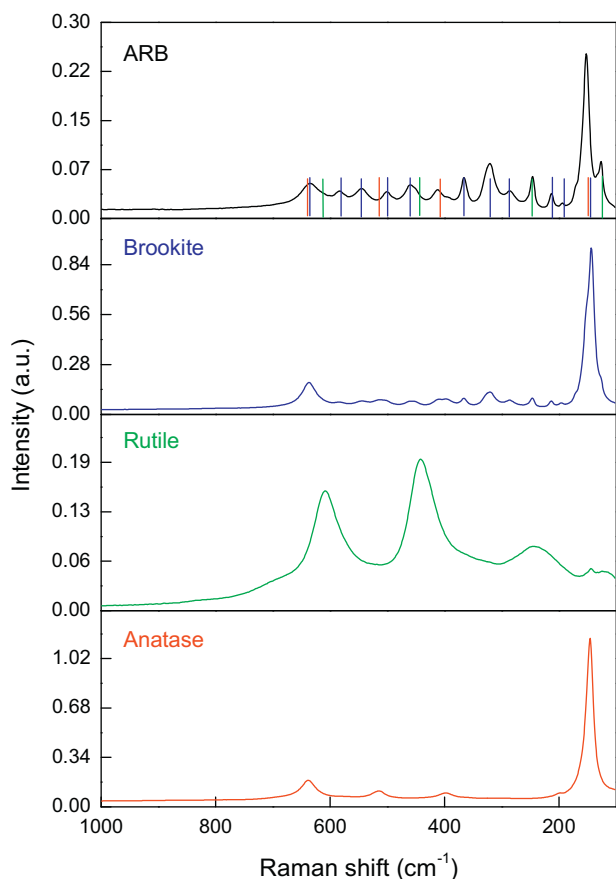


Fig. 4. Raman spectra of anatase, rutile, brookite and anatase/rutile/brookite (ARB) nanocomposite.

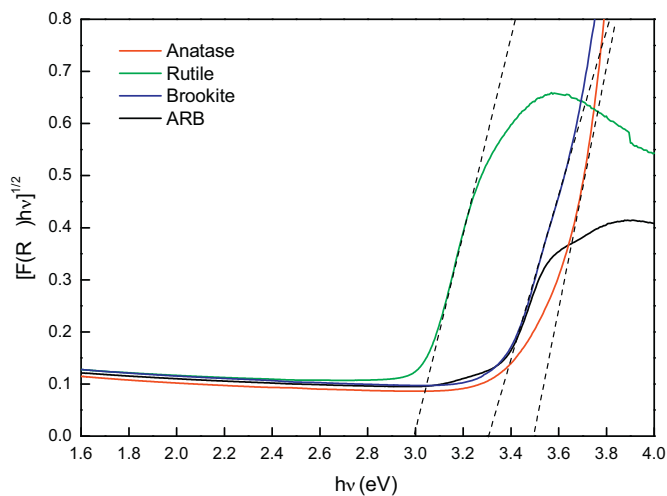


Fig. 5. Kubelka–Munk analysis of UV–vis diffuse reflection spectra of anatase, rutile, brookite and anatase/rutile/brookite (ARB) nanocomposite.

importance, since it enables to predict the behavior of particular polymorph in photocatalytic applications.

Acidic–basic properties of the individual TiO₂ polymorphs and ARB nanocomposite were evaluated by means of TPD method using *n*-propylamine as a probe molecule. Different properties of materials and consequently their behavior in advanced oxidation processes (including heterogeneous photocatalytic oxidation) can be attributed to various acidic–basic properties (i.e., amount and strength of surface acid sites). Fig. 6a presents TPD curves of pre-

pared oxides, with peaks in the low and high temperature range, as a result of desorption of *n*-propylamine from weak and strong acid sites. The obtained curves show that acidic–basic properties of the prepared materials vary significantly. Pure anatase shows high density of low to medium strength acid sites. Distribution of acid sites present on the surface of brookite is similar to that of anatase, but the amount is significantly lower. As opposed to the anatase and brookite, rutile shows the presence of strong acid sites with the highest peak positioned at 579 °C. Fig. 6a presents also a TPD curve of ARB nanocomposite, together with a theoretical curve calculated from the phase contents of singular phases within ARB sample, determined by means of XRD analysis. We can observe that the measured and calculated data differ significantly, which indicates that (i) a redistribution of acid sites strength occurs, and (ii) acidic–basic properties of ARB sample are not a linear combination of acidic–basic properties of singular polymorphs. In the ARB sample, the high temperature peak characteristic for strongly acid sites in rutile shifts to lower temperatures for about 100–130 °C. TPD curve of TiO₂ P25 Degussa is also displayed in Fig. 6a. When comparing the results of TiO₂ P25 Degussa, pure anatase and rutile, it is clearly visible that *n*-propylamine desorption peaks in low (the highest peak is positioned at 282 °C) and high (the highest peak at 569 °C) temperature ranges correspond to those of anatase and rutile, respectively. Furthermore, an influence of BET specific surface area on the amount of acid sites was observed. One can see in Fig. 6b that the total amount of acid sites is directly related to the BET specific surface area of the materials examined in this study; a linear relationship between the total acidity and BET specific surface area is demonstrated.

3.2. Photolytic and heterogeneous photocatalytic oxidation of BPA

Photocatalytic activities of pure TiO₂ polymorphs and ARB nanocomposite material were assessed by means of degradation of water dissolved model pollutant bisphenol A (BPA) under UV light irradiation for 60 min of operation. Fig. 7 demonstrates BPA conversion (to reaction intermediates, and CO₂ and H₂O) obtained in the presence of TiO₂-based photocatalysts in comparison to photolytic BPA oxidation (blank run). In any of heterogeneously photocatalyzed runs performed in this study, no dissolution of titania into the liquid phase was observed, which was verified by means of ICP-AES method. In order to determine adsorption equilibrium, all experiments underwent a dark period (30 min) prior to illumination with UV light. The reduction in concentration of BPA due to the adsorption on the surface of pure anatase and rutile amounted to 5 and 3%, while the obtained values for brookite and ARB solids were slightly higher, i.e., 17 and 15%, respectively. These data suggest that the brookite phase favors adsorption of BPA on its surface, comparing to other two pure polymorphs, which show significantly lower extent of adsorption. In the presence of TiO₂ P25 Degussa sample, uptake of BPA was very low (<1%). It is obvious from the reported data that strongly acid sites in rutile and TiO₂ P25 Degussa samples (Fig. 6) do not contribute to enhanced adsorption of BPA on the catalyst surface. The photolytic run, i.e., performed in the absence of a photocatalyst, demonstrated a photo-resistant character of BPA in the presence of UV light (Fig. 7), since low conversions were measured. On the contrary, the as-synthesized photocatalysts showed remarkable abilities for generation of OH• radicals responsible for degradation of BPA. After 60 min of photocatalytic oxidation conducted in the presence of ARB nanocomposite material, more than 94% conversion of BPA was attained, while in the presence of anatase, rutile, brookite and TiO₂ P25 Degussa samples we achieved 85, 23, 100 and 100% conversion of the selected model pollutant, respectively. Half-lives for the degradation of BPA (*t*_{1/2}) and the associated apparent first order rate constants (*k'*) were determined by applying the Langmuir kinetic model, with the

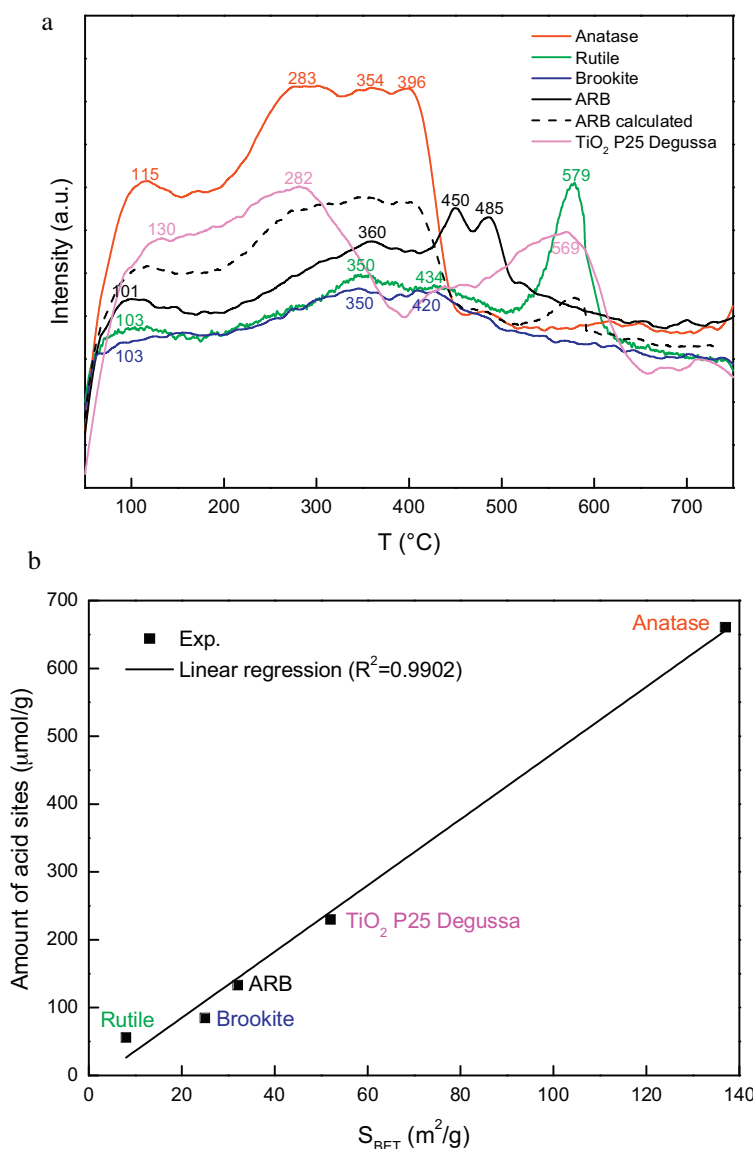


Fig. 6. (a) *n*-propylamine TPD curves for anatase, rutile, brookite and anatase/rutile/brookite (ARB) nanocomposite; (b) amount of acid sites vs. specific surface area (S_{BET}) of the prepared materials.

Table 2

Apparent first order rate constants (k') and corresponding half-lives ($t_{1/2}$) for photocatalytic degradation of aqueous solution of BPA under UV light.

Material	k' (1/min)	$t_{1/2}$ (min)
Anatase	0.036	19
Rutile	0.004	173
Brookite	0.108	6
ARB	0.044	16
TiO ₂ P25 Degussa	0.250	3

assumption that the reaction takes place on the surface of photocatalyst particles. The procedure is described in detail in our previous work [36]. The obtained $t_{1/2}$ values are summarized in Table 2.

The highest BPA conversion (Fig. 7) was achieved using brookite and TiO₂ P25 Degussa samples, which have the most balanced physico-chemical properties (the ideal ratio between the BET specific surface area and degree of crystallinity). Despite high activity toward BPA disappearance, brookite and TiO₂ P25 Degussa solids, as will be presented below, favor accumulation of reaction intermediates on their surfaces. Pure rutile particles suffer from the

low BET surface area combined with insufficient charge separation, resulting in a lengthy reaction half-life ($t_{1/2}$ = 173 min; Table 2). At the same time rutile is prone to bulk recombination of photo generated electrons and holes [16], since only the holes near the surface are able to migrate toward the surface. In contrast, in the case of anatase, surface hole trapping dominates because spatial charge separation is achieved by the migration of photo generated holes toward the particle surface due to the strong upward band bending what leads to effective separation of charge and thus slower recombination [16]. Brookite is also known as a very effective catalyst, when accordingly to Lin et al. [37] the demand of appropriate exposed facets is fulfilled. However, it is widely established that there are certain benefits of applying nanocomposites as photocatalysts, giving rise to suppressed charge recombination and, consequently, higher oxidation rates compared to pure phases. For instance, when anatase and rutile are in a form of a nanocomposite material, synergy can exist between these two physically contacted phases, like in TiO₂ P25 Degussa powder [38]. As proposed in our previous work [36], anatase generated electrons may migrate to rutile, causing a prolongation of charge carriers lifetime.

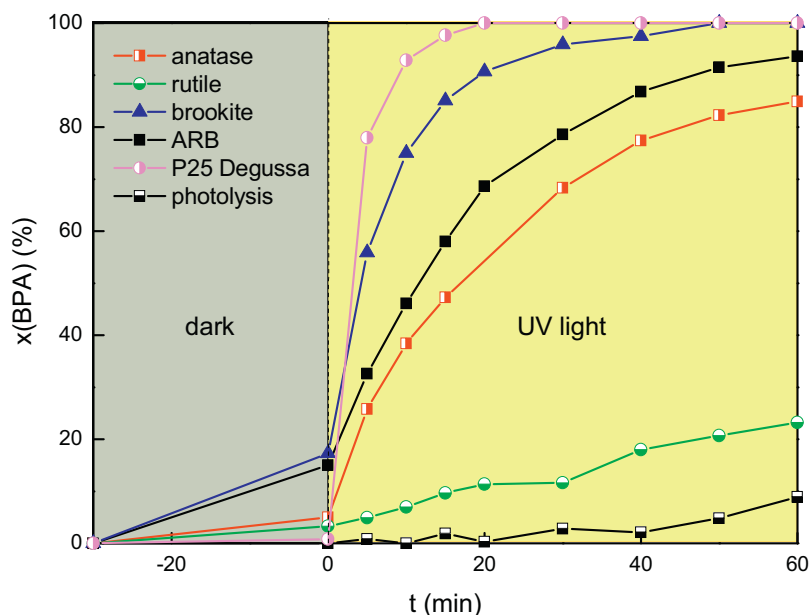


Fig. 7. Photolytic and photocatalytic degradation of aqueous solution of BPA in the presence of various catalysts. Reaction conditions: ambient pressure, $T=20^{\circ}\text{C}$, $c(\text{BPA})_0 = 10 \text{ mg/l}$, $V_0 = 250 \text{ ml}$, $\text{pH}_0 = 5.2$, $c(\text{catalyst}) = 125 \text{ mg/l}$, UVA light (150 W), $t_{\text{irradiation}} = 60 \text{ min}$.

Subsequently, this would favor formation of active species like hydroxyl radicals (via H_2O oxidation with photogenerated electron vacancies in the surface layers). Additionally, the contact between anatase and rutile might induce the relocation of hydroxyl radicals formed on the surface of anatase particles to rutile particles. In this way, the stripped anatase surface might be able to uptake newly generated OH^{\bullet} radicals, leading to higher concentration of these species at the surface of connected dissimilar-phase particles [36]. Further, a comparison of kinetic data shows that in the case of ARB nanocomposite which consists of three TiO_2 polymorphs (i.e., anatase, rutile and brookite), efficient charge separation was maintained. Over the AR nanocomposite examined in our previous work [36], $t_{1/2} = 15.1 \text{ min}$ was determined for photocatalytic oxidation of aqueous BPA solution. This data is very close to the $t_{1/2}$ value for ARB sample (Table 2), since both materials were prepared by similar catalyst preparation procedures. This observation alludes that the brookite phase doesn't contribute to further improvement of charge separation in the ARB nanocomposite.

There are several reports on the preparation of TiO_2 nanocomposite materials, but their activity rarely surpasses the activity of TiO_2 P25 Degussa, the well-known commercially available photocatalyst [39,40]. Herein, we confirmed that with single-phase photocatalysts only low to moderate rates of mineralization could be achieved, despite meaningful conversion rates of BPA (Fig. 7). Due to the fact that the degradation intermediates (or by-products) of AOPs might be even more hazardous toward fauna and flora than the parent organic pollutants, it is of great importance to achieve the highest possible mineralization extent (i.e., conversion to CO_2 and H_2O). Also, we have to take into consideration that measured TOC conversions in aqueous-phase samples do not consider the amounts of organic matter accumulated on the catalyst surface (which occur due to either of establishing sorption equilibrium or coking). Therefore, true TOC removals (obtained by subtracting accumulated TOC amounts from measured TOC values) were taken into account in this work when comparing catalyst mineralization potential. The results of apparent and true TOC removals (together with the amount of accumulated TOC) obtained in the presence of pure polymorphs (anatase, rutile, brookite), TiO_2 P25 Degussa and the as-prepared ARB nanocomposite are presented in Table 3. The latter also summarizes the amount of

carbon present on fresh and spent catalyst samples determined by means of CHNS analysis. Carbon elemental analysis demonstrated a direct correlation with accumulated TOC contents, which varied significantly upon sample surface chemistry. Among single-phase photocatalysts, anatase exhibited the highest true TOC conversion (22%), followed by negligible extent of mineralization achieved in the presence of rutile and brookite samples. This can be directly related to the physico-chemical properties of an individual catalyst. Besides the advanced activity of anatase due to the prolonged lifetime of charge carriers, its high BET specific surface area and abundant surface acid sites additionally govern the reaction of mineralization (Fig. 6). Despite the high activity of anatase, both commercial and synthesized ARB nanocomposite materials surpass the activity of singular phases. This data further underlines the welfares of applying nanocomposites as photocatalysts, giving rise to suppressed charge recombination and, consequently, higher mineralization rates compared to the pure phases.

Furthermore, we have discovered that despite longer half-life for BPA degradation in the case of ARB nanocomposite material compared to TiO_2 P25 Degussa sample (Table 2), the mineralization efficiency of the latter is notably lower. After 60 min of irradiation under UV light, 51 and 59% of BPA and its derivatives was mineralized in the presence of TiO_2 P25 Degussa and ARB solids, respectively. When the photocatalytic oxidation over ARB sample was further prolonged to 180 min, significantly, more than 92% of the initial pollutant was successfully transformed into CO_2 and H_2O (along with complete BPA conversion). Prolongation of UV irradiation time from 60 to 180 min in the presence of TiO_2 P25 Degussa resulted in 70.3% mineralization of BPA to CO_2 and H_2O . To some extent, amount of hydroxyl radicals generated by the present anatase and rutile phases proved to be sufficient for oxidation of accumulated organic matter, but as stated above, ARB solid showed higher oxidation ability, which can be attributed to the presence of brookite. Even though it was shown that the brookite sample favors carbon accumulation on its surface (both in dark and under UV light), this undesirable characteristic is not expressed within ARB material, where the brookite polymorph importantly contributes to the oxidation of liquid-dissolved reaction intermediates and organic matter accumulated on the catalyst surface (Fig. 7, Table 3). The outstanding activity of ARB nanocomposite can be

Table 3

The results of BPA removal, apparent TOC removal, accumulated TOC and real TOC removal using pure polymorphs (anatase, rutile, brookite), ARB nanocomposite material and commercially available TiO₂ P25 Degussa sample.

Material	^a BPA conversion (%)	Total organic carbon (TOC)			^c TC _{fresh} (mg/g)	^d TC _{spent} (mg/g)
		Apparent removal (%)	Accumulated (%)	Real removal (%)		
Anatase	85.0	29.0	7.3	21.7	0.66	1.12
Rutile	23.0	18.0	17.5	0.5	0.53	1.62
Brookite	100.0	26.0	26.0	0.0	0.34	2.00
ARB	94.0	80.0	20.8	59.2	0.49	1.78
	^b 100.0	100.0	7.8	92.2	0.49	0.98
TiO ₂ P25 Degussa	100.0	99.3	48.0	51.3	0.06	3.00
	^b 100.0	100.0	29.7	70.3	0.06	1.86

^a At $t = 60$ min.

^b At $t = 180$ min.

^c Amount of carbon on the surface of fresh catalyst samples, determined by means of CHNS analysis.

^d Amount of carbon on the surface of spent catalyst samples, determined by means of CHNS analysis.

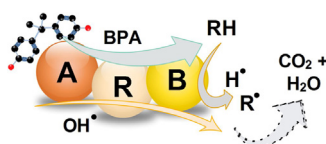


Fig. 8. Tentative reaction model of photocatalytic oxidation of aqueous BPA solution over anatase/rutile/brookite nanocomposite material.

associated with the occurrence of synergy between the present phases. Synergy can exist when different phases are separated but form agglomerates [41]; this is also the reason for high activity of TiO₂ P25 Degussa powder. Amount of TOC that was accumulated on the surface of ARB sample during the photocatalytic run, decreased with the prolongation of reaction time from 60 to 180 min (20.8 and 7.8%, respectively), which further emphasizes high oxidation potential of the prepared material. In our previous work, we have presented a nanocomposite TiO₂ material which consisted of 97% anatase and 3% rutile that enabled 94% BPA conversion after 60 min of UV irradiation, but no TOC conversion was attained [36]. This even further highlights the advantages of using three-phase mixed nanocomposite TiO₂ materials, since they enable both efficient charge separation and high potential for oxidation of reaction intermediates to carbon dioxide, which is crucial for achieving high mineralization rates.

Based on the above-presented results and discussion, we propose a tentative reaction model (Fig. 8) that describes BPA photocatalytic oxidation carried out in the presence of ARB nanocomposite. We believe that the very first reaction steps of BPA transformation to partially oxidized reaction intermediates occur by hydroxyl radicals formed on the most active and abundant surface sites (i.e., anatase). Charge separation in anatase particles is enhanced due to the presence of rutile polymorph in the ARB structure. The beneficial impact on photocatalytic activity of the synergistic effect between anatase and rutile TiO₂ phases was recognized also in other studies [42,43]. However, an increased separation efficiency of the photogenerated electron-hole pairs can be achieved also by combining different TiO₂ facets [44], and deposition of metal and non-metal species on the active surfaces [45]. Furthermore, liquid-dissolved reaction intermediates undergo stepwise oxidation (via the formation of short-chain carboxylic acids) to carbon dioxide and water, which occurs preferentially on brookite particles. It is believed that adsorption/activation of either aromatic or aliphatic reaction intermediates (denoted as RH in Fig. 8) occurs via hydrogen atom abstraction by brookite valence-band holes; hydroxyl radicals formed on the anatase surface are simultaneously involved in these reaction steps.

We have discovered that the presence of brookite in nanocomposite materials is beneficial, since the mixed-phase structure enables efficient charge separation and, importantly, increased resistance to accumulation of carbonaceous deposits, the latter being higher than observed for the benchmark TiO₂ P25 Degussa photocatalyst (composed of two polymorphs). The carbon-based mass balance indicates the potential of long-term photocatalytic mineralization of emerging organic pollutants over newly developed nanocomposite material comprising of anatase, rutile and brookite, due to significantly less expressed deposition of carbonaceous deposits on the catalyst surface. This is due to the fact that BPA molecules tend to accumulate onto most active and abundant metal oxide surface sites (i.e., anatase) [46], while the presence of brookite which favors adsorption/activation of reaction intermediates to enable mineralization, has a beneficial contribution to enhance the potential of nanocomposite materials for total oxidation of water dissolved organic pollutants.

4. Conclusions

In the presented work, we have described a simple synthesis route of sol-gel procedure with subsequent hydrothermal treatment at mild conditions (175 °C, 24 h) which led to the formation of highly uniform anatase/rutile/brookite nanocomposite TiO₂ material consisting of 43% anatase, 24% rutile and 33% brookite with BET specific surface area of 32 m²/g. Individual polymorph phases within the nanocomposite material crystallized separately and formed mixed agglomerates. All the TiO₂ polymorphs within the nanocomposite material are regularly shaped, where some of the anatase particles exhibit truncated octahedron morphology, rutile is in the form of tetragonal prisms with pyramidal termination and brookite is shaped as blocky particles, which are the smallest inside the nanocomposite material (~20 nm). Precursor material which was obtained after sol-gel synthesis step, was used also for the preparation of singular anatase, rutile and brookite TiO₂, which were used for the comparison purposes, to efficiently evaluate the advantages of suppressed charge recombination within the nanocomposite materials. Pure anatase possesses BET specific surface area of 137 m²/g and well developed structure in the form of nanofibers, rutile has the shape of humming-tops in micron size, which are composed of smaller nanocrystals and low BET specific surface area of 8 m²/g, while brookite is in the shape of curved nanocrystals with BET specific surface area of 25 m²/g. Photocatalytic activity of the prepared materials was evaluated in a UV light illuminated slurry reactor, where photocatalytic oxidation of an aqueous solution of priority pollutant bisphenol A was examined. It was determined that after 60 min of reaction in the presence of the as-synthesized nanocomposite material ARB, 94% conversion of BPA was achieved, while conversions in the presence of anatase,

rutile, brookite and TiO₂ P25 Degussa amounted to 85, 23, 100 and 100%, respectively. We confirmed that with single-phase photocatalysts only low to moderate rates of mineralization could be achieved, despite meaningful conversion rates of BPA. Regardless of the high activity of anatase and brookite for BPA degradation, both commercial and synthesized nanocomposite materials surpass the activity of singular phases. This data further underlines the prosperities of applying nanocomposites as photocatalysts, giving rise to suppressed charge recombination and, consequently, higher mineralization rates compared to the pure phases. After 60 min of irradiation under UV light, over 51 and 59% of BPA and its derivatives was mineralized in the presence of TiO₂ P25 Degussa and ARB solids, respectively. When the reaction over ARB was prolonged to 180 min, remarkably more than 92% of the initial pollutant content was effectively transformed into CO₂ and H₂O (along with complete BPA conversion). The exceptional activity and mineralization potential of ARB nanocomposite can be associated with the occurrence of synergy between the present phases.

Acknowledgement

The authors gratefully acknowledge the financial support of the Ministry of Education, Science and Sport of the Republic of Slovenia through Research program No. P2-0150.

References

- [1] S. Bakardjieva, V. Stengl, L. Szatmary, J. Subrt, J. Lukac, N. Murafa, D. Niznansky, K. Cizek, J. Jirkovsky, N. Petrova, J. Mater. Chem. 16 (2006) 1709.
- [2] G.K. Mor, K. Shankar, M. Paulose, O.K. Varghese, C.A. Grimes, Nano Lett. 6 (2006) 215.
- [3] D. Kuang, J. Brillet, P. Chen, M. Takata, S. Uchida, H. Miura, K. Sumioka, S.M. Zakeeruddin, M. Grätzel, ACS Nano 2 (2008) 1113.
- [4] D.P. Macwan, P.N. Dave, S. Chaturvedi, J. Mater. Sci. 46 (2011) 3669.
- [5] M. Auffan, M. Pedetour, J. Rose, A. Masion, F. Ziarelli, D. Borschneck, C. Chaneac, C. Botta, P. Chaurand, J. Labille, J.-Y. Bottero, Environ. Sci. Technol. 44 (2010) 2689.
- [6] Y. Liao, W. Que, Q. Jia, Y. He, J. Zhang, P. Zhong, J. Mater. Chem. 22 (2012) 7937.
- [7] A. Beltrán, L. Gracia, J. Andrés, J. Phys. Chem. B 110 (2006) 23417.
- [8] D.A.H. Hanaor, C.C. Sorrell, J. Mater. Sci. 46 (2010) 855.
- [9] R.I. Bickley, T. Gonzalez-Carreno, J.S. Lees, L. Palmisano, R.J.D. Tilley, J. Solid State Chem. 92 (1991) 178.
- [10] G. Sivalingam, K. Nagaveni, M.S. Hegde, G. Madras, Appl. Catal. B 45 (2003) 23.
- [11] K. Okamoto, Y. Yamamoto, H. Tanaka, A. Itaya, Bull. Chem. Soc. Jpn. 58 (1985) 2023.
- [12] T. Peng, D. Zhao, K. Dai, W. Shi, K. Hirao, J. Phys. Chem. B 109 (2005) 4947.
- [13] G. Liu, C. Sun, H.G. Yang, S.C. Smith, L. Wang, G.Q.M. Lu, H.-M. Cheng, Chem. Commun. (Camb.) 46 (2010) 755.
- [14] M. Liu, L. Piao, L. Zhao, S. Ju, Z. Yan, T. He, C. Zhou, W. Wang, Chem. Commun. 46 (2010) 1664.
- [15] J. Yu, H. Yu, B. Cheng, X. Zhao, Q. Zhang, J. Photochem. Photobiol. A 182 (2006) 121.
- [16] G. Li, K.A. Gray, Chem. Phys. 339 (2007) 173.
- [17] Q. Xiang, J. Yu, P.K. Wong, J. Colloid Interface Sci. 357 (2011) 163.
- [18] K. Ishibashi, A. Fujishima, T. Watanabe, K. Hashimoto, Electrochem. Commun. 2 (2000) 207.
- [19] Y. Liao, W. Que, Q. Jia, Y. He, J. Zhang, P. Zhong, J. Mater. Chem. 22 (2012) 7937.
- [20] S. Bakardjieva, J. Subrt, V. Stengl, M.J. Dianez, M.J. Sayagues, Appl. Catal. B 58 (2005) 193.
- [21] L. Miao, P. Jin, K. Kaneko, A. Terai, N. Nabatova-Gabain, S. Tanemura, Appl. Surf. Sci. 212–213 (2003) 255.
- [22] T.A. Kandiel, R. Dillert, A. Feldhoff, D.W. Bahnemann, J. Phys. Chem. C 114 (2010) 4909.
- [23] H. Zhao, L. Liu, J.M. Andino, Y. Li, J. Mater. Chem. A 1 (2013) 8209.
- [24] H. Xu, L. Zhang, J. Phys. Chem. C 113 (2009) 1785.
- [25] T. Paul, P.L. Miller, T.J. Strathmann, Environ. Sci. Technol. 41 (2007) 4720.
- [26] K. Doudrick, O. Monzón, A. Mangonon, K. Hristovski, P. Westerhoff, J. Environ. Eng. 138 (2011) 852.
- [27] M. Moonsiri, P. Rangsunvigit, S. Chavadej, E. Gulari, Chem. Eng. J. 97 (2004) 241.
- [28] P.-J. Chen, K.G. Linden, D.E. Hinton, S. Kashiwada, E.J. Rosenfeldt, S.W. Kullman, Chemosphere 65 (2006) 1094.
- [29] T. Yamamoto, A. Yasuhara, H. Shiraishi, O. Nakasugi, Chemosphere 42 (2001) 415.
- [30] V.N. Kuznetsov, N. Serpone, J. Phys. Chem. C 111 (2007) 15277.
- [31] K.S. Suslick, MRS Bull. 20 (1995) 29.
- [32] T.R. Esch, I. Gadaczek, T. Bredow, Appl. Surf. Sci. 288 (2014) 275.
- [33] H. Zhang, J.F. Banfield, J. Phys. Chem. B 104 (2000) 3481.
- [34] W.F. Zhang, Y.L. He, M.S. Zhang, Z. Yin, Q. Chen, J. Phys. D: Appl. Phys. 33 (2000) 912.
- [35] G.A. Tompsett, G.A. Bowmaker, R.P. Cooney, J.B. Metson, K.A. Rodgers, J.M. Seakins, J. Raman Spectrosc. 26 (1995) 57.
- [36] R. Kaplan, B. Erjavec, A. Pintar, Appl. Catal. A 489 (2015) 51.
- [37] H. Lin, L. Li, M. Zhao, X. Huang, X. Chen, G. Li, R. Yu, J. Am. Chem. Soc. 134 (2012) 8328.
- [38] T. Ohno, K. Sarukawa, K. Tokieda, M. Matsumura, J. Catal. 203 (2001) 82.
- [39] M. Qamar, C.R. Yoon, H.J. Oh, N.H. Lee, K. Park, D.H. Kim, K.S. Lee, W. Lee, S.J. Kim, Catal. Today 131 (2008) 3.
- [40] D.M.A. Alrousan, P.S.M. Dunlop, T.A. McMurray, J.A. Byrne, Water Res. 43 (2009) 47.
- [41] T. Ohno, K. Tokieda, S. Higashida, M. Matsumura, Appl. Catal. A 244 (2003) 383.
- [42] Y. Gao, H. Wang, J. Wu, R. Zhao, Y. Lu, B. Xin, Appl. Surf. Sci. 294 (2014) 36.
- [43] F. Xu, W. Xiao, B. Cheng, J. Yu, Int. J. Hydrogen Energy 39 (2014) 15394.
- [44] J. Yu, J. Low, W. Xiao, P. Zhou, M. Jaroniec, J. Am. Chem. Soc. 136 (2014) 8839.
- [45] M. Bellardita, A. Di Paola, L. Palmisano, F. Parrino, G. Buscarino, R. Amadelli, Appl. Catal. B 104 (2011) 291.
- [46] V.M. Gun'ko, V.V. Turov, Nuclear Magnetic Resonance Studies of Interfacial Phenomena, CRC Press, Florida, 2013, pp. 1040.